High-Resolution ENDOR Spectroscopy Combined with Quantum Chemical Calculations Reveals the Structure of Nitrogenase Janus Intermediate E4(4H)

Veronika Hoeke,[†] Laura Tociu,[‡] David A. Case,[§] Lance C. Seefeldt,[*,||] Simone Raugei,[*,⊥] and Brian M. Hoffman[*,†]

[†]Department of Chemistry, Northwestern University, Evanston, Illinois 60208, United States

[‡]Department of Chemistry, University of Chicago, Chicago, Illinois 60637, United States

[§]Department of Chemistry and Chemical Biology, Rutgers University, Piscataway, New Jersey 08854, United States

[||]Department of Chemistry and Biochemistry, Utah State University, Logan, Utah 84322, United States

[⊥]Physical Sciences Division, Pacific Northwestern National Laboratory, Richland, Washington 99352, United States

S *Supporting Information*

ABSTRACT: We have shown that the key state in N_2 reduction to two NH_3 molecules by the enzyme nitrogenase is $E_4(4H)$, the "Janus" intermediate, which has accumulated four $[e^-/H^+]$ and is poised to undergo reductive elimination of H_2 coupled to N_2 binding and activation. Initial ^1H and ^{95}Mo ENDOR studies of freeze-trapped $E_4(4H)$ revealed that the catalytic multimetallic cluster (FeMo-co) binds two Fe-bridging hydrides, [Fe−H−Fe]. However, the analysis failed to provide a satisfactory picture of the relative spatial relationships of the two [Fe−H−Fe]. Our recent density

E4(4H): Janus Intermediate

HH — *Hydride Protonation*

N2 H2 — *Reductive Elimination*

functional theory (DFT) study yielded a lowest-energy form, denoted as $E_4(4H)^{(a)}$, with two parallel Fe−H−Fe planes bridging pairs of "anchor" Fe on the Fe2,3,6,7 face of FeMo-co. However, the relative energies of structures $E_4(4H)^{(b)}$, with one bridging and one terminal hydride, and $E_4(4H)^{(c)}$, with one pair of anchor Fe supporting two bridging hydrides, were not beyond the uncertainties in the calculation. Moreover, a structure of V-dependent nitrogenase resulted in a proposed structure analogous to $E_4(4H)^{(c)}$, and additional structures have been proposed in the DFT studies of others. To resolve the nature of hydride binding to the Janus intermediate, we performed exhaustive, high-resolution CW-stochastic ^1H-ENDOR experiments using improved instrumentation, Mims ^2H ENDOR, and a recently developed pulsed-ENDOR protocol ("PESTRE") to obtain absolute hyperfine interaction signs. These measurements are coupled to DFT structural models through an analytical point-dipole Hamiltonian for the hydride electron−nuclear dipolar coupling to its "anchoring" Fe ions, an approach that overcomes limitations inherent in both experimental interpretation and computational accuracy. The result is the freeze-trapped, lowest-energy Janus intermediate structure, $E_4(4H)^{(a)}$.
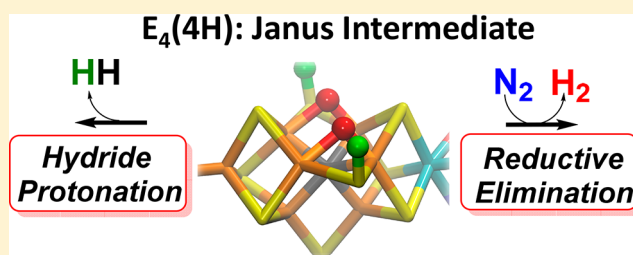
INTRODUCTION

The Mo-dependent nitrogenase enzyme system comprises two component proteins. The Fe protein delivers electrons one at a time to the MoFe protein, where they are utilized to reduce the substrate at the active-site iron−molybdenum cofactor ([7Fe-9S-Mo-C-R-homocitrate]; FeMo-co, Figure 1).[2,3] We have established the proposed Lowe−Thorneley (LT) kinetic model for the nitrogenase function, developed in the 1970s and 1980s,[2,4,5] which describes the kinetics of transformation among catalytic intermediates, denoted E_n, where n is the number of electrons delivered from the nitrogenase Fe protein to the catalytic FeMo-co of the MoFe protein (Figure 2). A defining feature of this scheme is the accumulation of $4[e^-/H^+]$ before N_2 is reduced and the obligatory formation and release of one mole of H_2 per mole of N_2 reduced, with a

limiting stoichiometry for enzyme-catalyzed nitrogen fixation given by eq 1,

$$N_2 + 8e^- + 16ATP + 8H^+ \rightarrow 2NH_3 + H_2 + 16ADP + 16P_i \tag{1}$$
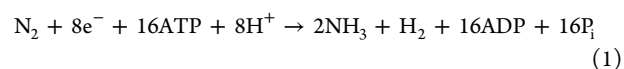
which implies a stoichiometric enzymatic requirement for $8[e^-/H^+]$ per N_2 reduced rather than the chemically required $6[e^-/H^+]$, a central feature that was both baffling and disputed and eventually even doubted by those who originally proposed it.[2]

The key state in this scheme is $E_4(4H)$, the "Janus" intermediate, which has accumulated four of the eight reducing equivalents required by eq 1: $E_4(4H)$ sits at a transition in the
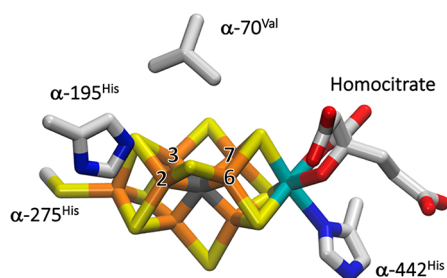
Figure 1. Crystal structure of FeMo-co. Fe is shown in rust, Mo in cyan, S in yellow, carbide in dark gray, carbon in light gray, N in blue, and O in red. The Fe atoms of the catalytic 4Fe-4S face are labeled 2, 3, 6, and 7. The α-275[Cys] and α-442[His] FeMo-co ligands along with two amino acids, α-70[Val] and α-195[His], that approach FeMo-co are also shown. The image was created using PDB coordinate 2AFI.
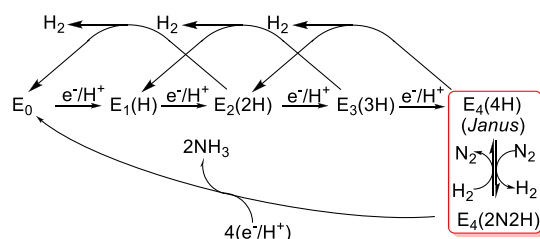

Figure 2. Simplified kinetic scheme for nitrogen reduction that focuses on the electron-accumulation and FeMo-co activation stages. E_n notation: n indicates the number of $[e^-/H^+]$ added to resting-state FeMo-co; the stoichiometry of H/N bound to FeMo-co is given in parentheses.

N_2 reduction pathway, Figure 2, poised to "fall back" to the E_0 resting state by the successive release of two H_2[6] but equally poised to eliminate H_2 and proceed to the reduction of N_2 to two NH_3 through the accumulation of four more equivalents, hence we have termed it "Janus".[7] We freeze-trapped and studied the Janus intermediate by EPR/ENDOR spectroscopies, showing that it has accumulated four reducing equivalents stored as two [Fe−H−Fe] bridging hydrides.[6,8,9] The location of the hydrides as bridges between Fe atoms plays a central mechanistic role. In a key contribution to catalytic efficiency, bridging hydrides are less susceptible to protonation than terminal hydrides, so they diminish the tendency of FeMo-co to "fall back" toward the resting state by a loss of reducing equivalents through hydride protonation and the formation of H_2 (Figure 2). However, opposing this benefit, the bridging mode likewise lowers the reactivity of these hydrides for N_2 reduction.[10,11]

The characterization of $E_4(4H)$ led to the experimental confirmation of the proposed stoichiometric requirement of eq 1 and to an understanding of the fundamental mechanistic role of the hydrides through the recognition that the enzyme can be activated for N≡N binding and triple-bond cleavage only through the reductive elimination (re) of H_2.[7,12,13] We showed[13] that the triple bond cleavage proceeds through a near-thermoneutral reductive elimination/oxidative addition (re/oa) equilibrium, as pictured in Figure 2. This process was subsequently explored through a computational analysis[14] based on broken symmetry (BS) density functional theory (DFT) calculations. These showed how the $E_4(4H)$ enzyme state mechanistically couples exothermic H_2 formation and release to the endothermic cleavage of the N_2 triple bond to create the near-thermoneutral re/oa equilibrium: re of the

hydrides generates an H_2 complex, but as inferred from experiment,[15] H_2 is lost *only* when displaced by N_2, leading to an end-on Fe−N_2 complex that proceeds to the diazene-level $E_4(2N2H)$ intermediate.[7,12,13]

These computations are distinguished by their exploration of the size and character of the computational model required to accurately describe the *re* activation of nitrogenase. They showed that to obtain an accurate picture it is necessary to include all of the residues and waters interacting directly with FeMo-co, via both specific H-bond interactions and non-specific electrostatic interactions of FeMo-co with its environment, and that not all of these are evident from a mere inspection of the available crystal structures. However, these DFT calculations revealed the presence of various possible E_4 isomers that are close in energy, which differ in the location of the four cofactor-bound hydrogens of $E_4(4H)$,[14] and whose ordering is sensitive to the adopted DFT flavor, as highlighted in recent reports.[14,16,17] Moreover, notorious issues related to the single-determinant nature of BS DFT, which result in a solution that is a superposition of states with a given secondary spin quantum number $m_S = S$ rather than a proper pure spin state S,[18,19] add further uncertainty to the energy ordering of computationally identified E_4 isomers. In fact, the energies of the proper pure spin states can be quite different from the BS DFT energies.

Because of the central role of $E_4(4H)$ as the culmination of the electron-accumulation phase of the nitrogenase cycle and the starting point for the key *re* of H_2 and reduction of N_2, it is of the highest importance to characterize its nature. Our original ^1H ENDOR study concluded that FeMo-co in $E_4(4H)$ binds two metal-bridging hydrides, [Fe−H-M], based on the observation of spin delocalization onto the H and an analysis of the anisotropic hydride hyperfine coupling tensors with an analytical description for a nucleus that is located at an arbitrary position relative to two spin-coupled paramagnetic metal ions and that interacts by through-space dipolar coupling with each of these "anchor" ions.[20,21] When combined with the results of a subsequent ^{95}Mo ENDOR study,[22] this treatment ruled out molybdenum as an anchor metal, thus implying the presence of two [Fe−H−Fe] bridging hydrides.[22] Since then, this analytical treatment of bridging hydrides has been supported through its successful application to biomimetic inorganic hydrides, both terminal and metal-bridging.[23−25]

The initial ^1H ENDOR study of $E_4(4H)$ showed that the two [Fe−H−Fe] bridges have very similar electronic properties. It further showed that they are differently oriented relative to the g-tensor of FeMo-co, but the analysis was unable to provide a satisfactory picture of the relative spatial relationships of the two bridging moieties.[9] Our DFT study of the *re/oa* equilibrium yielded as the lowest-energy form of $E_4(4H)$ the structure $E_4(4H)^{(a)}$ shown in Figure 3 with parallel Fe−H−Fe planes bridging two pairs of "anchor" Fe on the Fe2,3,6,7 face of FeMo-co.[14] Slightly higher in energy was structure $E_4(4H)^{(b)}$, with one bridging and one terminal hydride, and still higher was $E_4(4H)^{(c)}$, in which a single pair of anchor Fe supports two bridging hydrides, a "dihydride[16] dibridge". However, the differences in energy between these states were not beyond the uncertainties of the calculation, and a structure of the VFe protein obtained by Einsle and co-workers indeed led them to propose a dibridge structure analogous to $E_4(4H)^{(c)}$.[26,27] Finally, a quite different "open" structure, $E_4(3H;CH)$, with one [Fe−H−Fe] bridging hydride and a protonated interstitial carbide rather than a second hydride,
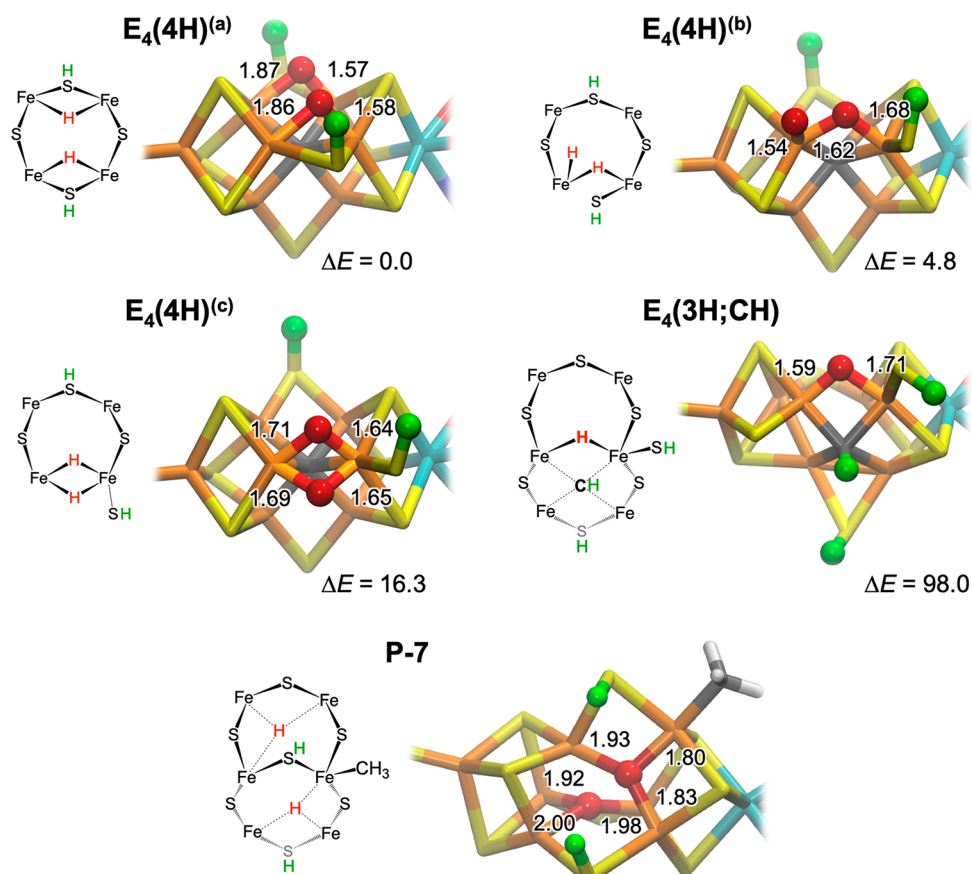
Figure 3. Lowest-energy structures of the Janus intermediate as seen in recent density functional theory computations,[13] $E_4(4H)^{(a,b,c)}$, plus a high-energy structure with a singly protonated carbide that has been proposed on the basis of other computations, $E_4(3H;CH)$,[26−29] and the P-7 structure proposed by Siegbahn,[26,17] which results from the accumulation of 7[e−/H+]. The relative electronic energies (ΔE in kJ/mol calculated at the DFT/BP86 level) for $E_4(4H)^{(a,b,c)}$ and $E_4(3H;CH)$ along with selected Fe−H distances (in angstroms) from ref 13 are provided. Fe−H distances for P-7 from ref 17 are also given. Note that the Fe−H distances in [Fe−H−Fe] are not typically equal. Irons are shown in rust, molybdenum in cyan, carbon in gray, sulfurs in yellow, protic hydrogens in green, and hydrides in red.

denoted as $E_4(3H;CH)$, was found at quite high energy. Other DFT studies proposed this structure to play a critical role in nitrogenase activity.[28−31] Siegbahn further suggested that $E_4(3H;CH)$ is the precursor of an Fe-bound methyl intermediate where FeMoco has accumulated 7[e−/H+], denoted here as P-7 (referred to as E_5^0 in ref 29), which was proposed to be the central catalytic species that undergoes *re* of H_2.[28,29]

To resolve the nature of hydride binding to the Janus intermediate, we have carried out extensive high-resolution ^{1}H ENDOR measurements using the resolution-enhancing "stochastic"[32] CW-ENDOR protocol performed on instrumentation greatly improved since our original study.[9] These are complemented by the use of a recently developed pulsed-ENDOR procedure to obtain absolute signs for hyperfine couplings[33] and by Mims pulsed ^{2}H ENDOR measurements. These measurements are coupled to the structural DFT models through the use of the analytical point-dipole Hamiltonian for the electron−nuclear dipolar interaction of the hydride to its "anchoring" Fe ions, a powerful approach that overcomes limitations inherent in both experimental interpretation and computational chemistry accuracy. The result of this protocol is the identification of the lowest-energy structure of the Janus intermediate: $E_4(4H)^{(a)}$ (Figure 3).

MATERIALS AND METHODS

Materials and Protein Purification. All reagents were obtained from Sigma-Aldrich (St. Louis, MO) or Fisher Scientific (Fair Lawn, NJ) and were used without further purification. Argon, N_2, and acetylene gases were purchased from Air Liquide America Specialty Gases LLC (Plumsteadville, PA).

The $E_4(4H)$ intermediate has been characterized and behaves similarly in three *Azotobacter vinelandii* MoFe variants: wild type,[34,13] singly substituted α-70[Ile], and doubly substituted α-70[Val→Ile]/α-195[His→Gln] MoFe protein.[9] Because use of the variants permits the freeze trapping of MoFe with higher populations of $E_4(4H)$,[9] experiments were carried out both with the singly and doubly substituted MoFe protein. The enzymes were purified and samples were prepared as has been described.[35]

ENDOR Spectroscopy. Q-band CW ENDOR spectra were collected at 2 K on a spectrometer[36] that had been upgraded with a low-noise microwave amplifier; temperature 2 K was achieved with a helium immersion Dewar. Relaxation effects in the original "Feher-style" CW ENDOR protocol[1,37,38] (100 kHz field modulation; phase-sensitive detection of the dispersion, rapid-passage signal; 2 K) were overcome here by the use of Stochastic ENDOR, as first reported by Brueggeman and Niklas,[39] which is a hybrid method that employs field-modulated CW-EPR but pulsed rf.[32] Further improving signal-to-noise ENDOR spectra collection employed broadening of the rf to 100 kHz.[40] Q-band pulsed Mims and Davies ENDOR spectra[41] were collected at 2 K on a spectrometer with a helium immersion Dewar as previously reported[42] The Mims ENDOR intensities exhibit nulls (suppression holes) when $A\tau = n$ ($n = 0, 1, 2,...$),[41] where A is the

hyperfine coupling (A) and τ is the time between the second and third microwave pulses in the three-pulse sequence.

For a single molecular orientation and for nuclei with nuclear spin I = 1/2 (^{1}H), the ENDOR transitions for the $m_S = \pm$ 1/2 electron manifolds are observed, to first order, at frequencies $\nu_\pm = |\nu_n \pm A/2|$, where ν_n is the nuclear Larmor frequency and A is the orientation-dependent hyperfine coupling. At the low- and high-field edges of the EPR spectrum (g_1 and g_3, respectively), ENDOR interrogates a single molecular orientation ("single-crystal-like" position). The complete hyperfine tensor principal values and their orientations relative to **g** are obtained by analyzing a 2D field-frequency ("orientation-selective") pattern of ENDOR spectra taken at numerous fields across the EPR envelope, as described.[43−45] ENDOR simulations were performed in MATLAB with the easyspin (v 5.0) toolbox.[46]

Signs of the hyperfine couplings (more specifically, the sign of $g_{Nuc}A_{Nuc}$) were obtained by the PESTRE protocol,[33] a pulsed-ENDOR multisequence comprising multiple Davies ENDOR sequences, carried out in three distinct experimental phases: (I) an EPR saturation phase (rf off) of 100 Davies sequences whose spin−echo intensities quickly converge to the steady-state "baseline" (BSL); (II) 24 sequences, each of which contains a fixed rf frequency; and (III) an EPR recovery phase (rf off) of 388 sequences during which the spin echo intensity of the spin system polarized by the ENDOR transitions induced in II, the dynamic reference level (DRL), relaxes to BSL. When $A_{Nuc} > 0$ (and $g_{Nuc} > 0$), if ν_+/ν_- is being interrogated, the DRL relaxes to the BSL from below/above. When $A_{Nuc} < 0$, the opposite behavior is observed.

Density Functional Theory Calculations. The structure of the E_4 isomers investigated in the present study (Figure 3) was taken from previous BS-DFT calculations.[14] All structures were obtained for an electron count for E_0 in the [$Mo^{3+}3Fe^{2+}4Fe^{3+}$] oxidation state.[18,19] The adopted structural model of the active site comprises 198 atoms and includes FeMo-co with truncated modifications of the α-275^{Cys}, α-442^{His} ligands (*Azotobacter vinelandii* numbering), *R*-homocitrate, and *all* of the MoFe protein residues and water molecules that engage hydrogen-bonding interactions with the FeMo-co or are known to be important in the catalytic activity (α-70^{Val} and α-96^{Arg}).

■ RESULTS

ENDOR Spectroscopy of the Hydrides in E_4(4H). The implementation of the stochastic ENDOR protocol, coupled with the improved spectrometer sensitivity, yields spectra of remarkable resolution with strong orientation selection, as illustrated in Figure 4. A full 2D field-frequency ^{1}H stochastic
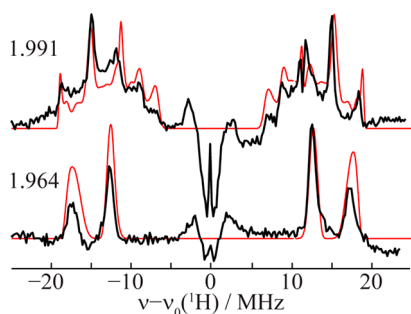

Figure 4. ^{1}H stochastic-field modulation (35 GHz) detected (stochastic CW) ENDOR spectra of E_4(4H) acquired at g = 1.991 and 1.964 (black) and simulations generated as described below (red). The signal with $\nu_0(^1H) \pm \sim3$ MHz, with both positive and negative features, represents transient responses from weakly coupled, more distant protons.[1] *Experimental conditions*: microwave frequency, 35.045 GHz; modulation amplitude, 2.7 G; microwave power, 1 μW; rf power, 10 W; temperature, 2 K; stochastic sequence (sample/delay/rf), 1/3/3 ms; the bandwidth of the rf excitation was broadened to 100 kHz.

CW ENDOR pattern has been collected across the EPR envelope for E_4(4H) in H_2O and D_2O buffers, and the extent of the improvement is seen by comparison with the 2D pattern reported previously (Figure S1). However, before presenting the new 2D pattern, we first navigate a "decision tree" that leads to the assignment of the features within the spectra to one of the two hydrides, H1 and H2. This in turn enables the analysis of the 2D pattern in terms of the magnitudes and relative signs of the two hyperfine coupling tensors. We then describe the determination of the absolute signs of these tensors and, central to this report, the relative orientations of the principal axes of the two tensors. Finally, we employ the analytical anchor model for the anisotropic hyperfine coupling tensor of a bridging hydride, which allows us to use the symmetries of the [Fe−H−Fe] hyperfine tensors and their relative orientations for H1 and H2 to distinguish among the proposed structures for the E_4(4H) intermediate (Figure 3).

Alternative Models for ^{1}H ENDOR Patterns. As shown in Figure 5A, the single-crystal-like ^{1}H ENDOR spectra of E_4(4H) collected at g_1 and g_3 show hyperfine-split doublets from two strongly coupled protons; the peaks disappear in samples prepared in D_2O (not shown), showing that these hydrons are exchangeable. The resolution of two signals immediately shows that the two protons are magnetically inequivalent, with different hyperfine-tensor orientations and/ or principal values. However, as shown below, at intermediate fields the responses from the two protons spread and overlap strongly. As a first "branch-point" in a decision "tree" for determining the hyperfine tensors, one must correlate the signals denoted as H1 and H2 at g_1 with the two signals at g_3 (Figure 5A). In one alternative, A(H1) > A(H2) at both g_1 and g_3 (i.e., the signals of the two hydrides at the extremal g values do not "cross"). In the second alternative, the signals do cross (i.e., A(H1) > A(H2) at g_1 but A(H1) < A(H2) at g_3).

As a second branch-point, we revisit our previous assignment of these two strongly coupled ^{1}H ENDOR signals to two [Fe−H−Fe] bridging hydrides with rhombic anisotropic coupling tensors by considering all possible assignments of these two signals to terminal and bridging hydrides. Studies of crystallographically characterized inorganic complexes[23−25] have thoroughly validated our previous assumption that a terminal hydride yields an approximately axial hyperfine tensor, whereas a bridging hydride is expected to give a hyperfine tensor whose anisotropic component is nearly rhombic. There are four alternative models for assigning the binding mode to the two distinct hydridic species bound to FeMo-co (Figure 5B): Both hydrides may be terminal (denoted **T/T**) or bridging (**B/B**); one hydride may be terminal and the other bridging, which itself comprises two cases differing in the assignment to H1 and H2 (**T/B** or **B/T**). In addition, for each of these four models, the hydride signals can evolve as the magnetic field is moved across the EPR envelope according to either a crossing or noncrossing scenario.

As described in the SI, a painstaking process of simulation/ analysis has established that the hydride ^{1}H spectra obey the crossing **B/B** model. Overlaid on the 2D pattern of ENDOR spectra in Figure 6 are sums of optimized simulations that employ the parameters for this model that are listed in Table 1. Figure S5 displays the 2D pattern and simulations of Figure 6 as well as the 2D pattern overlaid with the individual simulations for the two hydrides. These provide the basis for determining the listed signs of the hyperfine interactions, which are established in the next subsection.
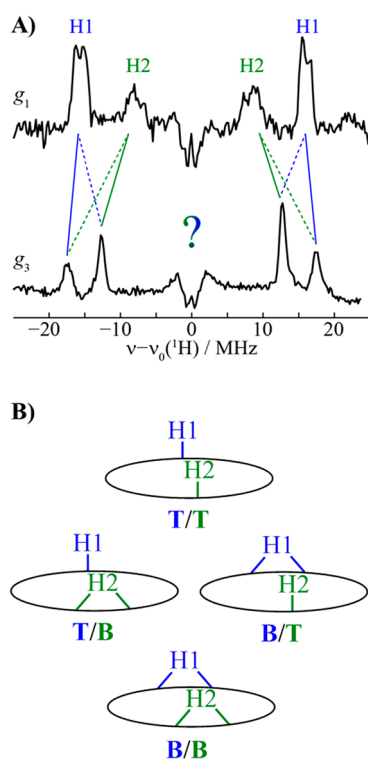
Figure 5. (A) Single-crystal-like ENDOR spectra collected at g_1 and g_3. (Slight splittings in H1 peaks at g_1 indicate that the rigorous single-crystal limit has not been reached.) The figure illustrates the two possible scenarios by which the hydride signals can evolve across the EPR envelope in a 2D field-frequency pattern of ENDOR spectra collected from g_1 to g_3. In the first scenario, the patterns of H1 and H2 do not cross at intermediate fields (i.e., A(H1) > A(H2) at g_1 and A(H1) > A(H2) at g_3 (solid lines)). In the second scenario, the patterns of H1 and H2 do cross at intermediate fields so that A(H1) > A(H2) at g_1 but A(H1) < A(H2) at g_3 (dashed lines)). (B) Alternative models for hydride binding to FeMo-co, where a 4Fe4S face is depicted as an oval. Both hydrides may be terminal (model denoted as **T/T**) or bridging (**B/B**), or the intermediate may contain one terminal and one bridging hydride, denoted as **T/B** or **B/T** depending on the assignment to H1 or H2 (see part A). For each of these four models, either of the two "crossing" scenarios illustrated in A can be obtained, leading to a total of 8 possible bases for the 2D field-frequency plot.

The two hyperfine tensors have nearly equal isotropic components, and both anisotropic (traceless) tensor contributions not only are completely rhombic, namely, with one null component and the remaining two components having equal magnitude and opposite signs, but also have equal-magnitude nonzero components for the two hydrides. Of central importance to this study is the relative orientation of these two tensors, to which we return below. As can be seen in Figure 6, the simulations generated with the hyperfine tensors listed in Table 1 provide a remarkably precise correspondence with the *extremely* high resolution experimental stochastic CW spectra across the 2D pattern plus the scaled 2H spectra. For completeness and for use below, Figure S5 shows both the 2D pattern with summed simulations and the same pattern showing the individual simulations for H1 and H2.

Absolute Signs of Hydride Hyperfine Couplings. Earlier, it was impossible to obtain absolute signs of the H1 and H2 hyperfine couplings, and thus of a_{iso}, or the relative orientations of the positive/negative components of the two
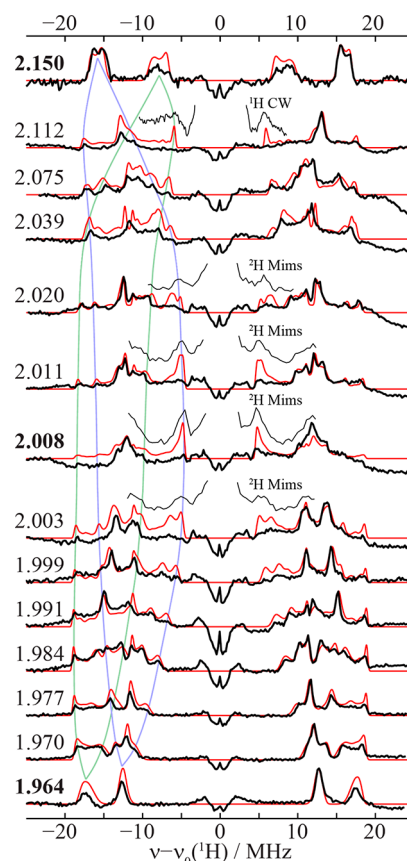
Figure 6. Full 35 GHz ^{1}H stochastic CW field-frequency ENDOR pattern for E$_4$(4H). Experimental data (black) and sum of simulations for ^{1}H1 and ^{1}H2 (red), normalized at each g value. Curves running across the 2D plot were added as a guide to the eye, connecting the outer edges of ^{1}H1 (blue) and ^{1}H2 (green) spectral features along the different g values. Simulation parameters (**B/B** model) are listed in Table 1. At selected g values, a complementary ^{1}H field-swept CW or ^{2}H Mims ENDOR spectrum (thinner line; ^{2}H spectra were collected on D$_2$O turnover samples and scaled to ^{1}H frequencies by factor $g_N(^1H)/g_N(^2H) = 6.5$) is shown to illustrate the match of experiment and simulation in the low-frequency region; for further ^{2}H measurements, see Figure S12. The following experimental conditions were used. ^{1}H stochastic CW ENDOR: the same as in Figure 4. ^{1}H field-swept CW ENDOR: microwave frequency, 35.036 GHz; modulation amplitude, 0.7 G; microwave power, 1 μW; rf power, 10 W; rf scan speed, 1 MHz/s; temperature, 2 K; and bandwidth of the rf excitation broadened to 100 kHz. ^{2}H Mims ENDOR: 34.890 GHz; $\pi/2$ = 50 ns; τ = 400 ns; t_{rf} = 30 μs; repetition time, 50 ms; temperature, 2 K.

Table 1. Experimentally Determined [Fe−^{1}H−Fe] ^{1}H Hyperfine Coupling Parameters for E$_4$(4H)

	hydride	
	H1	H2
A[a]	+[11.6, 24.8, 38.0]	+[35.6, 9.2, 22.4,]
T	[−13.2, 0.0, +13.2]	+[13.2, −13.2, 0.0]
a_{iso}	+24.8	+22.4
$[\alpha, \beta, \gamma]$[b]	0, 20, 20	10, 30, 0

[a] ^{1}H hyperfine tensor component, with an uncertainty of ∼0.1 MHz. [b] Euler angles $[\alpha, \beta, \gamma]$ defined according to the *zyz* convention describe the rotation of the **A** eigenframe away from the **g** reference frame; with an uncertainty of ≲2−3°.

anisotropic interactions. We do so here through use of the PESTRE multi-Davies sequence-pulsed ENDOR protocol for determining hyperfine signs[33] (Materials and Methods). This protocol involves monitoring an ENDOR transition from the nucleus in question through the application of a Davies ENDOR multisequence at a fixed rf frequency and thus requires a measurement at frequencies where the responses of the two hydrides do not overlap. The assignment of ENDOR peaks to H1 and H2 is simple in the spectra collected at the edges of the EPR signal (Figures 6 and S5), but these fields also have the lowest ENDOR signal intensity, and as a result, the PESTRE response at these fields is not readily obtained. However, the excellent resolution and precise simulation of the new ^{1}H ENDOR data allow us to identify ENDOR features associated with an individual hydride even in spectra at intermediate g values, where the overall patterns of the two hydrides overlap extensively (Figures 6 and S5 and S10). Thus, at $g = 1.977$ ^{1}H1 exhibits an isolated sharp peak with $\nu_+ = 65.5$ MHz whose ^{1}H Davies ENDOR response (Figure 7A) is
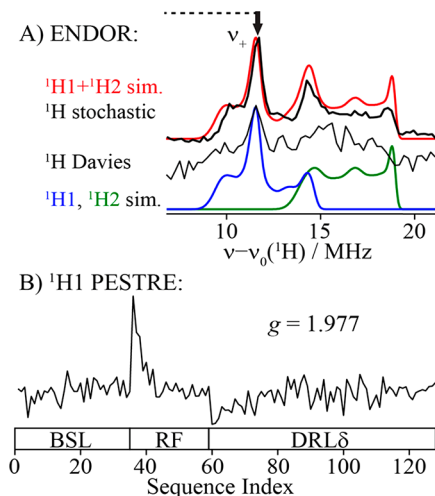

Figure 7. Absolute hyperfine sign determination for hydride H1 by PESTRE at $g = 1.977$. (A) 35 GHz ^{1}H stochastic CW (thicker black line) and Davies (thinner black line) ENDOR responses around the ν_+ branch of the ^{1}H1 doublet, and sum (red) and separate ^{1}H1 (blue) and ^{1}H2 (green) simulations. Simulation parameters (B/B model) are listed in Table 1. (B) ^{1}H PESTRE trace collected from the ν_+ branch of the ^{1}H1 doublet. The following experimental conditions were used. (A) ^{1}H stochastic CW ENDOR: the same as in Figure 4. ^{1}H Davies ENDOR: microwave frequency, 34.776 GHz; $\pi = 60$ ns; $\tau = 450$ ns; $t_{rf} = 35$ μs; repetition time, 100 ms; temperature, 2 K. (B) The same as in A (^{1}H Davies) except for the repetition time of 200 ms and the rf frequency of 65.5 MHz.

strong enough to obtain a ^{1}H PESTRE trace. In the corresponding ^{1}H1 PESTRE trace, shown in Figure 7B, the ν_+ DRLδ intensity in the PESTRE multisequence relaxes to the BSL level from *below*, which for ^{1}H ($g_N > 0$) implies $A > 0$. Because the magnitude of A is governed by a_{iso}, this means that $a_{iso} > 0$ for ^{1}H1.

In the ^{1}H ENDOR spectrum at g_2, both branches of the ν_+/ν_- doublet for H2 exhibit features that are isolated from H1 signals and that have sufficient intensity to yield satisfactory ^{1}H PESTRE traces (Figure 8). As required, the two branches give opposite DRL responses: the ν_- DRLδ relaxes to the BSL from *above*, whereas the ν_+ DRLδ relaxes from *below*. This again implies that $A > 0$ and $a_{iso} > 0$ for the ^{1}H2 nucleus. This result
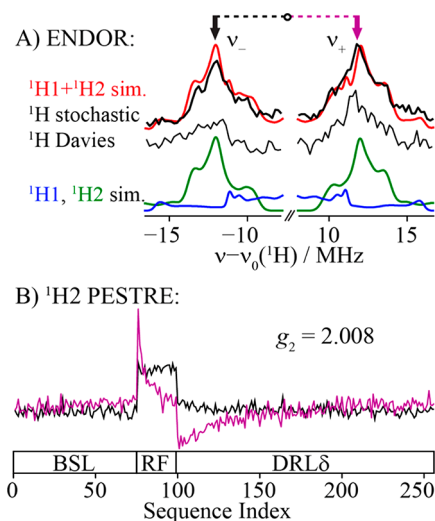

Figure 8. Absolute hyperfine sign determination for hydride H2 by PESTRE at $g_2 = 2.008$. (A) 35 GHz ^{1}H stochastic CW (thicker black line) and Davies (thinner black line) ENDOR responses around the ν_- (black arrow) and ν_+ (purple arrow) branches of the ^{1}H2 doublet and sum (red) and separate ^{1}H1 (blue) and ^{1}H2 (green) simulations. Simulation parameters (B/B model) are listed in Table 1. (B) ^{1}H PESTRE traces collected from the ν_- (black) and ν_+ (purple) branches of the ^{1}H2 doublet. The following experimental conditions were used. (A) ^{1}H stochastic CW ENDOR: the same as in Figure 4. ^{1}H Davies ENDOR: microwave frequency, 34.757 GHz; $\pi = 80$ ns; $\tau = 600$ ns; $t_{rf} = 35$ μs; repetition time, 50 ms; $t_{mix} = 5$ μs; and temperature, 2 K. (B) The same as in A (^{1}H Davies) except for the 150 ms repetition time and the 41.1 (ν_-) and 64.7 (ν_+) MHz rf values.

was confirmed by an additional ^{1}H PESTRE measurement of the $\nu_+ = 70.8$ MHz signal from ^{1}H2 at $g = 1.970$ (Figure S11).

With the hyperfine signs as determined from the ^{1}H PESTRE measurements, the present ENDOR measurements and analysis provide signed hydride hyperfine tensors with extraordinary precision. The result is hyperfine tensors for ^{1}H1 and ^{1}H2 whose anisotropic components **T** not only are fully rhombic, namely, with each exhibiting a null component $[t, 0, -t]$ but also exhibiting identical, although permuted, principal values within the precision of these measurements (Table 1). We emphasize that the tabulated couplings naturally arise from the fitting rather than being imposed as a constraint on the fitting. The hydrides are not, however, chemically identical; the isotropic components, although similar, are not identical: $a_{iso} \approx$ +22 and +25 MHz for H1 and H2, respectively. The availability of both magnitudes and signs of the hydride couplings provides a strong constraint on computations of the geometric and electronic structure of the hydride-bound FeMo-co of E_4(4H), as will be seen below.

Relative Orientations of the H1/H2 Hyperfine Tensors. The small values for the Euler angles relating the hyperfine tensor of each hydride to the **g**-tensor axis frame (Table 1) imply that the hyperfine (**A**), and thus the anisotropic dipole-coupling (**T**), tensors of both hydrides are essentially coaxial with **g** and thus are themselves coaxial; indeed, Table 2 (below) explicitly shows that each of the three corresponding pairs of principal axes for the hyperfine couplings of the two hydrides subtends an angle of only a few degrees. However, although the anisotropic tensors for the two hydrides have components with identical values, as noted above, these values are permuted with respect to each other

Table 2. Angles between Corresponding H1/H2 Components of the H1, H2 Rhombic Dipolar Tensors[a]

	$\{-t(H1)\|+t(H2)\}$	$\{0(H1)\|-t(H2)\}$	$\{+t(H1)\|0(H2)\}$	$\{0(H1)\|0(H2)\}$
experiment	13	10	11	85
		$E_4(4H)^{(a)}$ (∓) (+/+)		
BP86[b]	12	11	11	84
B3LYP	16	11	16	81
		$E_4(4H)^{(c)}$ (∓)		
BP86	23[b]	47	45[b]	78[c]
B3LYP	54[b]	46	46[b]	100[c]
		$E4(4H)^{(c)}$ (+/+)		
BP86	51	48[b]	23[b]	57
B3LYP	49	46	56	65

[a]Signs in headings for DFT results, such as (∓), indicate the signs of t_1 and $t2$. Estimated uncertainties in experimental angles are ∼4−5°. Reversing all signs yields equivalent results. [b]The calculated angles are the complement; an angle and its complement are experimentally indistinguishable. [c]These angles are fixed by the (∓) signs to equal the dihedral angle between [Fe−H−Fe] planes.

$(A3(H1) \leftrightarrow A1(H2); A1(H1) \leftrightarrow A2(H2); A2(H1) \leftrightarrow A3(H2))$, as indicated in Chart 1, which shows that the

Chart 1. ¹H Tensor Permutations
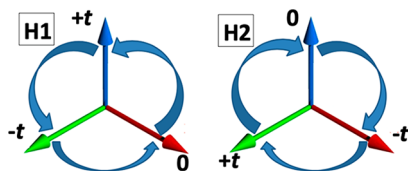
clockwise permutation of the tensor components of H1 yields tensor H2 and the counterclockwise permutation of the H2 components yields tensor H1, Stated alternatively, each hydride has dipole components $[\pm(t = 13.2\ \text{MHz}); 0]$ but the permutation of the tensor components orients the axes of the tensor so that parallel (‖) components are as follows: $\{-t(H1)\|+t(H2)\}$, $\{0(H1)\|-t(H2)\}$, $\{+t(H1)\|0(H2)\}$. The differences in the 2D patterns for H1 and H2, not least the differences in the single-crystal-like spectra at g_1 and g_3, arise primarily because of this permutation. Of central importance, through an analysis presented below, the permuted relative orientations of the components of the coaxial tensors provide the basis for distinguishing among the possible structures of the Janus intermediate presented in Figure 3.

ENDOR Spectroscopy of S−H Protons of $E_4(4H)$. According to the kinetic model for nitrogenase catalysis,[2,4,5] FeMo-co accumulates a proton as well as an electron at each stage of reduction, with the four $[e^-/H^+]$ at the $E_4(4H)$ stage taking the form of the two bridging hydrides and two protons. To directly examine exchangeable proton sites without interference from ¹H signals associated with nearby residues, we recorded a 2D field-frequency pattern of ²H Mims ENDOR spectra on the D_2O turnover sample (Figure S12). As described in the SI, an analysis of these signals shows they can be confidently attributed to either an $(SH)^-$ bridge or a terminal −SH formed through cleavage of one Fe−S bond.[14] We note that an $(^1H-S^-)$ released from the cluster and moved more than ∼7 Å away[47] would instead give an extremely small ¹H coupling, $A < 1$ MHz.

Analysis of Anisotropic Hyperfine Couplings. *Hyperfine Couplings to Metal Hydrides.* Our work with enzymatic intermediates and inorganic complexes with both terminal and bridging hydrides[23−25] has taught us the characteristic signatures of hydrides bound to paramagnetic metal centers. (i) They exhibit large isotropic couplings that for the high-spin

ions of FeMo-co would primarily arise from spin delocalization into the M−H bond(s), exactly as seen here. (ii) The anisotropic hyperfine coupling tensor of a terminal hydride exhibits a "dipolar" form, $\mathbf{T} \approx [-t, -t, 2t]$, where the unique direction corresponds to the M−H vector. (iii) The anisotropic coupling to a hydride interacting with two metal ions depends jointly on the distances to the two anchor M distances and on their spin. When the spin on the second metal is small and/or its distance to the hydride is much larger than to the first, the anisotropic coupling can approach the dipolar form of a terminal M−H. However, in sharp contrast, a rhombic coupling, $\mathbf{T} \approx [-t, 0, t]$ is a definitive signature of a hydride bridge that has significant interactions with both anchor metal ions.

Point-Dipole Approaches. Our studies have further shown that we can accurately calculate the dipolar tensor of a hydride, $\mathbf{T}$, bound to ions of a multinuclear center by summing the through-space point-dipole interactions with each paramagnetic center M_i (Fe, Mo),

$$\mathbf{T} = \sum_i \mathbf{T}_i, \ \mathbf{T}_i = t_i \mathbf{M}_i, \ t_i = (K_i d_i)\left(\frac{2g\beta g_n\beta_n}{r_i^3}\right) \quad (2a)$$

where the 3×3 matrices $\mathbf{M}_i$ incorporate the orientation of the M_i−H vector relative to the FeMo-co molecular frame. The weight, t_i, of an individual $[M_i-H]$ point dipole is determined by three factors: (1) a dipolar term, which depends on fundamental constants and the inverse cube of the M_i−H distance, r; (2) the covalency parameter d_i ($0 < d_i \leq 1$) (i.e., the fraction of the unpaired spin density, ρ_i, of an ion of spin S_i that remains on the ion after it undergoes covalent interactions with its ligands), as obtained from a BS-DFT computation, $d_i = |\rho_i|/2S_i$; and (3) the vector-coupling coefficient, K_i, for ion i obtained from the spin-coupling model for FeMo-co in which its total spin is determined by exchange coupling between metal ions. The point-dipole approach is particularly appropriate for nitrogenase and other enzymes that involve high-spin Fe ions because, to a first approximation, they should be spherical "balls of spin" —exactly so for Fe^{III} ($S = 5/2$) and very nearly so even for Fe^{II} ($S = 2$)—and thus behave like point dipoles when interacting with distant nuclei.

For FeMo-co, one can numerically diagonalize the matrix $\mathbf{T}$ to obtain predicted principal values for the observed cluster anisotropic coupling tensor,

$$\mathbf{T} = [T_1, T_2, T_3] \quad (3)$$

along with the orientation of that tensor relative to the molecular frame. Instead, in the anchor approach, this information is obtained from the dominant contributions to eqs 2 and 3 (i.e., the interactions of an [Fe−H−Fe] hydride with its two anchoring FeMo-co Fe ions). The anchor model is reliable for a multimetallic cluster such as FeMo-co because t_i exhibits an r^{-3} dependence on the distance r between the metal ion and hydride: the longer distances between a hydride and the nonanchor metal ions minimize the interactions with these other ions and, consequently, their contribution to the full sum over ions (eqs 2). This expectation was supported by a comparison of the calculations with the anchor-model equations of eqs 4 to an implementation of eq 3 for test-case, spin-projected ($S = 1/2$) DFT-derived states for $E_4(4H)^{(a)}$.

[Fe−H−Fe] Bridge. A signal benefit of the anchor approach to an [Fe−H−Fe] moiety is that the sum of dipolar interactions between two Fe atoms and a bridging hydride at an arbitrary relative position, Chart 2, yields analytic equations

Chart 2
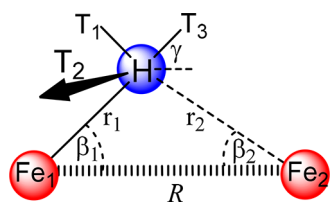
for the components of the tensor, **T**, and the tensor orientation, eqs 4,[20,21,48]

$$\mathbf{T} = t_1\mathbf{M}_1 + t_2\mathbf{M}_2 = t_1\left(\mathbf{M}_1 + \left(\frac{t_2}{t_1}\right)\mathbf{M}_2\right)$$
(4a)

$$T_3 = \frac{1}{2}t_1\left[\left[\frac{\left(1 + \left(\frac{t_2}{t_1}\right)\right)}{2}\right] + \frac{3}{2}\frac{1}{\cos 2\gamma}\left(\cos 2\beta_1 + \left(\frac{t_2}{t_1}\right)\cos 2\beta_2\right)\right]$$
(4b)

$$T_2 = -\frac{1}{2}t_1\left[1 + \left(\frac{t_2}{t_1}\right)\right]$$
(4c)

$$T_1 = -(T_3 + T_2)$$
(4d)

$$\tan 2\lambda = \frac{\left[\sin 2\beta_1\left(\frac{t_2}{t_1}\right)\sin 2\beta_2\right]}{\left[\cos 2\beta_1 + \left(\frac{t_2}{t_1}\right)\cos 2\beta_2\right]}$$
(4e)

Components T_1 and T_3 lie in the [Fe−H−Fe] plane, rotated away from the Fe−Fe axis by an angle γ about the normal to that plane (T_2). (T_3 lies along that axis for $\gamma = 0$.) These equations reveal that both the relative magnitudes of the components of the anisotropic coupling tensor and the tensor orientation (eq 4e) depend on the geometry of the center (expressed here in terms of the two internal angles β_1 and β_2) and a single spin/structure-dependent parameter—the ratio of t_i for the anchor metal ions, t_2/t_1—while the absolute signs and values of the components scale with the t_1 parameter.

It is straightforward to solve the analytical equations for the anchor model for conditions under which the dipolar tensor,
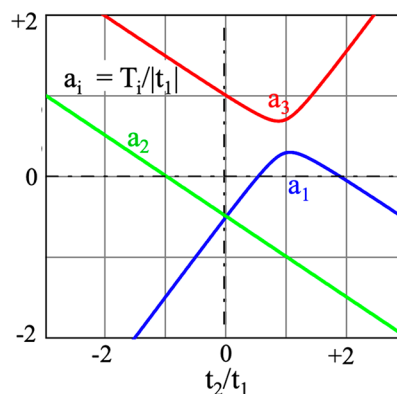

Figure 9. Reduced dipolar tensor components, $a_i = T_i/t_1$, calculated as a function of t_2/t_1 for a hydride bridge with $R = 2.52$ Å, $r_1 = 1.65$, and $r_2 = 1.69$. The two a_1 nulls give similar angles, γ.

T, becomes fully rhombic, namely, has one null component. As illustrated in Figure 9, which plots the "reduced" tensor components given by eqs 4,

$$a_i = T_i/t_1$$

for a typical DFT-determined bridging hydride geometry, there are two distinct scenarios in which the signature rhombic symmetry of the hyperfine tensors of the two (**B/B**) $E_4(4H)$ hydrides (Table 1) can be precisely matched by the tensor arising from the interactions of a hydride bridge with the spins of its two anchor Fe ions.

(i) When t_1 and t_2 have opposite signs and **T** is rhombic because $t_1 = -t_2$ (eq 4c and Figure 9), the null tensor element is T_2, oriented along the normal to the [Fe−H−Fe] plane (eq 4c, Chart 3). This imposes an exact constraint on the ratios of

Chart 3
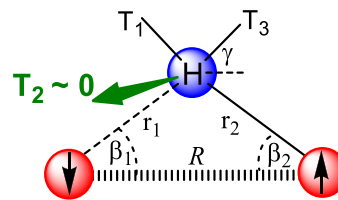
the K_id_i products in terms of the ratio of the Fe−H distances, r_i:

$$T_2 = 0 \Rightarrow \left(\frac{t_2}{t_1}\right) = -1, \quad \frac{|K_2d_2|}{|K_1d_1|} = \left(\frac{r_2}{r_1}\right)^3$$
(5)

The two nonzero components T_2 and T_3 have opposite signs and equal magnitudes and are rotated around the normal/T_2 by the angle γ (eq 4d)

(ii) If t_1 and t_2 have the same sign, $t_2/t_1 > 0$, then solving eqs 4 for a null tensor element is often possible (but not always; see Figure 9). For all plausible FeMo-co [Fe−H−Fe] geometries and ratios t_2/t_1, there are at most two values of t_2/t_1 that yield a null T_1 component (e.g., Figure 9), which lies in the Fe−H−Fe plane (Chart 4). The two nonzero components T_2 and T_3 have opposite signs and equal magnitudes (eq 4d), $T_2 = -T_3$, determined by specifying
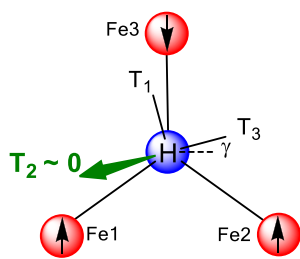
Chart 4
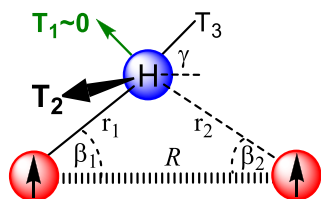
either of the two t_i values. Finally, T_1 are T_3 are rotated by an angle γ (eq 4e). Such a situation has been seen for delocalized mixed-valence Fe_2 complexes.[23,25]

[Fe$_3$−H] Triangle. The P-7 structure recently proposed by Siegbahn[29] has two hydrides, each lying roughly in the plane of three Fe ions (Figure 3, Chart 5). Although we show below

Chart 5

that the question of whether this model can describe $E_4(4H)$ is ultimately decided by other arguments, for completeness we note that the anchor model can even provide guidance in considering the hyperfine couplings of such a moiety. Thus, if $t_3 = -(t_1 + t_2)$, then the dipolar tensor is rhombic with $T_2 = 0$, and if t_1, $t_2 > 0$ (as shown), then $T_1 = -T_3 > 0$ and $0 \leq \gamma \leq 15°$. However, if (t_1, t_2) are of opposite sign, then γ approaches $\pm45°$ depending on which one is greater in magnitude.

Testing the Janus Structural Models. The central goal of this study is the discrimination among computationally proposed structures of the $E_4(4H)$ ($S = 1/2$) Janus intermediate (Figure 3). We do so by integrating BS-DFT-derived structures with the key characteristics of the $E_4(4H)$ intermediate obtained from high-resolution ENDOR experiments. These key characteristics shown in this report are the following: (i) There are two metal hydrides bound to the FeMo-co cluster, and they exhibit nearly identical hyperfine tensor components. (ii) The tensors are very closely coaxial (and coaxial with **g**). (iii) The two hyperfine tensors are dominated by large, nearly equal isotropic couplings. (iv) The anisotropic hyperfine interaction tensors, **T**, for the two hydrides are perfectly rhombic within experimental error (**B/B** 2D ENDOR pattern). (v) Although the components of the two anisotropic tensors have the same magnitudes, the signed tensor components of one hydride are "permuted" with respect to each other, with the correspondence between the components of the two hydride tensors summarized in Table 2 and Chart 1.

The analysis presented below focuses primarily on the relative orientations of the signed hyperfine components of the rhombic H1 and H2 hyperfine tensors. With this approach, we need not employ fine details of the BS-DFT spin densities to calculate tensor components, a task that approaches, and indeed likely passes, their limits of reliability. Instead, to determine whether a BS-DFT state with a given arrangement

of two hydrides (Figure 3) is capable of reproducing the permuted rhombic tensors of experiment, one need only incorporate into the anchor equations the [Fe−H−Fe] geometries for each hydride, which are robustly determined, solve for the t_i that yield a rhombic dipolar tensor for each, and then compare the calculated relative orientations with experiment (Figure 9 and Table 2).

Calculations with this protocol first show that it is robust against quite substantial variations in the structure of the Fe−H−Fe fragment. Second, the protocol eliminates any residual uncertainties caused by the limitations of the BS-DFT energetics and the secondary contributions from spins on the other Fe ions: the experimental tensors indeed are rhombic, and this procedure reproduces their symmetry by construction. Finally, as noted above, the anchor equations are supported by comparisons with anisotropic DFT tensors obtained by summing the dipolar interactions with all of the metal ions. The relevant metric and electronic structure parameters of the FeMo-co E_4 states visualized in Figure 3 and used in the protocol are listed in Table S1, which includes structural data obtained from DFT calculations using both BP86 and B3LYP exchange and correlation functionals;[14] the comparisons with experiment are carried out for structures generated with both functionals.

$E_4(4H)^{(a)}$ with Parallel Hydride Bridges. For both BP86 and B3LYP functionals, the lowest-lying structure is $E_4(4H)^{(a)}$, which features two bridging hydrides, [Fe2−H1−Fe6] and [Fe3−H2−Fe7] (Figure 3). In $E_4(4H)^{(a)}$, the planes of the [Fe2−H−Fe6] and [Fe3−H−Fe7] hydride bridges are essentially orthogonal to the Fe2,3,6,7 face and nearly parallel to each other, with the angle between their normals (dihedral angle between [Fe−H−Fe] planes) being only $\tau \approx 10°$ (Table S1). Both functionals predict a cluster of BS states with essentially the same geometry and only slightly different energy (within 20 kJ/mol from the lowest-energy solution) yet differing in the orientations of the anchor Fe spins.[14]

For each functional, there are states within this cluster of BS solutions that cannot satisfy the experimental restrictions on the dipolar interaction tensors of the two (Chart 1; see also Tables 1 and 2). For example, we find anchor spin patterns $(t_2; t_6)(t_3; t_7) = (-/-)(-/-)$, where each hydride bridges Fe atoms with parallel spins (as in Chart 4), and $(\mp)(\pm)$, where each hydride bridges Fe atoms with antiparallel spins (as in Chart 3). These BS states yield two nearly identical hydride hyperfine tensors, with positive a_{iso} and coaxial rhombic dipolar tensors, but the corresponding tensor components are nearly parallel rather than permuted (Chart 1). However, the cluster of low-lying BS solutions also includes states where the [Fe2−H−Fe6] hydride has antiparallel anchor spins, implying opposite signs of their dipolar coupling parameters, $(t_2; t_6) \leftrightarrow (-/+)$, while the [Fe3−H−Fe7] hydride has parallel anchor spins, with $(t_3; t_7) \leftrightarrow (+/+)$, as schematized in Chart 6. When this spin arrangement exhibits two hydrides with tensors of rhombic symmetry, the [Fe2−H1−Fe6] hydride has its null tensor component normal to its Fe−H−Fe plane ($T_2 = 0$) with $T_3 < 0$; the [Fe3−H2−Fe7] hydride has $T_1 = 0$ and $T_3 > 0$ (both in-plane). The tensors are rotated about the normal to their [Fe−H−Fe] normal (T_2 direction) by an angle, γ, that ranges from 31 to 54° for the two functionals (Table 2).

Thus, by examining the patterns of signs of the interaction parameters t_i in combination with DFT-computed $E_4(4H)^{(a)}$ geometries as inputs into the anchor equations, we can predict the relative orientations of rhombic [Fe2−H−Fe6]/[Fe3−H−

Chart 6
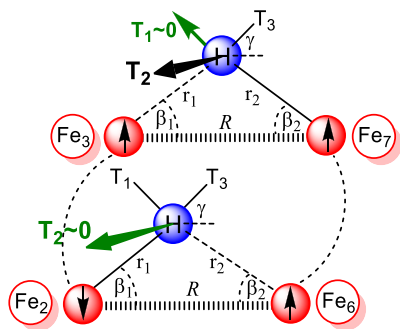
Fe7] hydride tensors that are possible for a structure, thereby determining whether a model (Figure 3) exhibits tensors that match the experimentally determined angles between the corresponding tensor components of H1 and H2. As can be seen from the results reported in Table 2, tensors for $E_4(4H)^{(a)}$ as computed using the structure from the DFT functional and the anchor signs $(-/+)$ for $[Fe2-H1-Fe6]$ and $(+/+)$ for $[Fe3-H2-Fe7]$ accurately reproduce the experimentally observed coaxial, rhombic dipolar coupling tensors with nearly parallel permuted components, and near-orthogonal nulls, as drawn in Chart 6.

$E_4(4H)^{(c)}$ Dihydride Dibridge. $E_4(4H)^{(c)}$ (Figure 3) features a dihydride dibridge with both hydrides anchored by Fe2 and Fe6. Again, both functionals give a cluster of BS solutions with essentially the same geometric structure differing only slightly in energy,[14] with members of the cluster exhibiting both parallel [e.g., $(+/+)$] and antiparallel [e.g., $(\mp)$] Fe2/Fe6 anchor spins determining the signs of the t_i. In the parallel case, a rhombic tensor for each hydride must have the null component lying in its $[Fe-H-Fe]$ plane, while in the antiparallel case, the null is normal to its plane. With both BP86 and B3LYP functionals, the anchor-model dipolar tensor for each hydride is rotated around the normal to its $[Fe-H-Fe]$ plane by an angle of $\gamma \sim 45°$; in the computational models, the two planes are rotated relative to each other about the Fe–Fe vector with large dihedral angles (BP86, 77.7°; B3LYP, 99.7°). As above for the $E_4(4H)^{(a)}$ structure, we have calculated the angles between the near-coaxial permuted component of the calculated rhombic hydride dipolar tensors for both parallel $(+/+)$ and antiparallel $(\mp)$ spin orientations (signs of t_i). As can be seen from the results reported in Table 2, the calculated angles between corresponding components of the permuted tensors for the $E_4(4H)^{(c)}$ structure, whether considering states with $(+/+)$ or $(\mp)$ anchor Fe, strongly disagree with the experimentally determined angles, and in addition, the null components are not orthogonal for the $(+/+)$ configuration. This violation of the experimental constraints on the relative tensor orientations provides strong evidence against such a structure for $E_4(4H)$.[49]

$E_4(4H)^{(b)}$. This structure contains one Fe2–H–Fe6 bridging hydride and one terminal hydride on Fe2 (Figure 3). Application of the anchor model to this structure shows that it cannot yield a rhombic tensor for both hydrides: even if the bridging hydride does exhibit a rhombic tensor, the other would exhibit the dipolar-type tensor of a terminal hydride. Thus, this structure spectroscopically would correspond to the **T/B** and **B/T** models for the ^1H ENDOR patterns, which have been ruled out above. In short, this model is incompatible with experiment and cannot describe the Janus intermediate.

$E_4(3H;CH)$. The $E_4(3H;CH)$ structure is no less readily dismissed by comparison to the present experiments. This structure contains only one hydride, in a nearly symmetrical bridging $[Fe2-H-Fe6]$ arrangement (average Fe–H distance, 1.65 Å). The central carbide of the resting FeMo-co is protonated, with the resulting C–H fragment nearly symmetrically coordinated "above" a square plane of the four Fe atoms, Fe2, 6, 4, 5, on the surface of the "exploded" FeMo-co cluster $[Fe_4(CH)]$, with the $[Fe2-H-Fe6]$ hydride roughly lying in this plane.

To begin, the DFT computations show that the C–H fragment has essentially zero spin density. Thus, this ^1H atom would not have the large isotropic coupling associated with H1 and H2 seen experimentally (Table 1). The C–^1H hydrogen will undergo through-space anisotropic dipolar couplings to the four pseudoanchor Fe ions that bind the carbon. However, a consideration of a pseudoanchor model that incorporates only couplings to the Fe of the Fe_4 plane (or of the more complete of eq 3) indicates that it would be impossible for the diagonalized sum of these couplings to yield a rhombic tensor whose components are equal to those of the hydride bridge, but permuted. In fact, the dipolar coupling components for the C–^1H hydrogen will be much less than to the hydride bridge. The $[Fe2-^1H-Fe6]$ bridge is nearly symmetric, with an average Fe–^1H distance of 1.65 Å, whereas the average distance between the ^1H bonded to the C and Fe ions of the Fe_4 anchor base is 2.64 Å. Thus, for sets of Fe d_i spin coefficients (eq 2a) for the two hydrides with comparable values needed to achieve rhombic dipolar tensors, the difference in distances would make the magnitudes of the Fe–H dipolar coupling t_i parameters for the pseudoanchors of the C–^1H much smaller than those for the anchors of the bridging hydride, $|t_i(Fe_4)/t_j(bridge)| \approx 1/4$, and the resulting nonzero dipolar tensor components for C–^1H would be correspondingly smaller. Indeed, with both a small a_{iso} and a small dipolar coupling for such a C–^1H moiety, if one were present then it would be expected to give ENDOR signals that fall within the signals from the –SH protons rather than correspond to one of the H1 or H2 Fe-bound hydrides.

Thus, we conclude that ^1H of a $E_4(3H;CH)$ C–^1H fragment cannot give a hyperfine tensor—neither isotropic nor dipolar contributions—that matches that of the hydride bridge as seen in experiment and that $E_4(3H;CH)$ and similar models with a singly protonated carbide do not describe the Janus $E_4(4H)$ intermediate.

P-7. This model can be dismissed on the basis of only the properties of $E_4(4H)$ and its reactivities. (i) $E_4(4H)$ has accumulated $4[e^-/H^+]$ as cleanly shown by its return to E_0 by two sequential steps of hydride protonation with the overall loss of two H_2 molecules.[6] Instead, P-7 has accumulated $7[e^-/H^+]$ and cannot return to E_0 by the loss of two H_2 molecules. (ii) $E_4(4H)$ is an odd-electron system with $S = 1/2$ whose EPR spectrum is well established[9,13] and whose ENDOR properties we report here in detail; P-7 has an even number of electrons and thus an integer spin (proposed as $S = 0$), which is incompatible with the experimental evidence. (iii) $E_4(4H)$ undergoes an experimentally observed, kinetically facile, near-thermoneutral conversion to the EPR-active $(S = 1/2)$ $E_4(2N2H)$ through re loss of H_2 and the binding/reaction of N_2; re by P-7 would create an even-electron state (also proposed as $S = 0$), which is again incompatible with experiment.

The relaxation of $E_4(4H)$ to E_0 needs further elaboration. The proposal that the P-7 state, with seven accumulated $[e^-/H^+]$, is the Janus intermediate (the state that binds N_2 upon *re* of H_2) instead of $E_4(4H)$, with four accumulated $[e^-/H^+]$, is embedded in a mechanism that involves the activation of the true E_0 through the accumulation of $5[e^-/H^+]$ to generate a state, which we will denote as P-5 (referred to as $A_5{}^0$ or $E_3{}^0$ in ref 29), after which the enzyme cycles through an $8[e^-/H^+]$ catalytic process that begins and ends with P-5 and produces $2NH_3$. However, no such preactivation process has been observed in the many pre-steady-state measurements carried out over the years.[2,4] Moreover, a two-step relaxation of the even-electron P-7 with the release of two H_2 molecules would produce the even-electron P-3, whereas the measurements of the relaxation of the odd-electron $S = 1/2$ $E_4(4H)$ with the release of $2H_2$ unambiguously show that it relaxes directly to the EPR-active odd-electron E_0 ($S = 3/2$) resting state. The structure of this state has been beautifully revealed as having a trigonal-prismatic Fe_6C core with intercalated carbide,[50] not the EPR-silent (or integer-spin) P-5 state with a peripheral iron-bound methyl group as would be required by such a mechanism. And there is no doubt that $E_4(4H)$ indeed relaxes to the E_0 state. That the crystalline E_0 and the putative E_0 formed by $E_4(4H)$ relaxation are identical is established by the identity of the EPR spectra of the solution E_0 formed by relaxation and that of the crystalline E_0, both of which precisely match the long-established EPR spectrum of as-isolated Mo-nitrogenase.

■ SUMMARY AND CONCLUSIONS

Exceptionally high resolution 2D field-frequency 35 GHz ^1H ENDOR patterns confirm and highly refine our previous reports that the $E_4(4H)$ nitrogenase Janus intermediate contains two $[Fe-H-Fe]$ bridging hydrides and in addition characterizes the protons bound to sulfides that accompany the bridging hydrides. A detailed analysis of 2D field-frequency ENDOR patterns shows that the hydrides exhibit nearly identical hyperfine tensor components (Table 1). The tensors are dominated by large, nearly equal isotropic couplings, and the signs of the isotropic couplings have been established for the first time. The components of the anisotropic hyperfine interaction tensors determined here for the two $E_4(4H)$ hydrides are identical and perfectly rhombic within experimental error (**B/B** 2D ENDOR pattern). Such rhombic dipolar interactions are a signature of bridging hydrides, as established in studies of enzyme active sites[20] and model studies.[23−25] ^{95}Mo ENDOR studies showed that the ^{95}Mo hyperfine coupling for this intermediate is about 5-fold too small for Mo to be an anchor metal ion of either hydride, leaving two Fe atoms as the only possible anchors for each of two $[Fe-H-Fe]$ hydride bridges.

The anisotropic tensors of the two hydrides are nearly coaxial and have identical components, but the tensor components of one hydride are permuted with respect to those of the other, a property captured by noting the near-orthogonality of the equivalent tensor components for the two hydrides and corresponding, nearly exact coaxiality of the permuted components (Table 2). The determination of the absolute signs of the tensor components for each of the two hydrides, as presented in the table, is of particular importance in relating these tensors to structure.

These experimental findings were complemented by a careful theoretical analysis of structural models of the $E_4(4H)$ state. The broken-symmetry DFT calculations of $E_4(4H)$ identified $E_4(4H)^{(a)}$, where two hydrides bridge the Fe2/Fe6 and Fe3/Fe7 pairs of atoms, as the lowest-energy isomer. However, variations between different flavors of DFT exchange and correlation functionals, while having a small impact on geometries, can appreciably affect the energy ordering.[14,16,17] These considerations, along with the inability of DFT to accurately describe multireference electronic systems, such as FeMo-co, make it difficult to determine the nature of $E_4(4H)$ based on DFT-derived relative energies alone. To overcome these limitations, the present spectroscopic properties have been combined with DFT calculations to test five possible structures for the Janus intermediate (Figure 3: $E_4(4H)^{(a)}$, $E_4(4H)^{(b)}$, $E_4(4H)^{(c)}$, $E_4(3H;CH)$, and P-7), primarily through use of a model hyperfine Hamiltonian based on a point dipolar interaction with the electron spins of the anchoring Fe ions. The spectroscopic signatures for each of these structures have been assessed and compared with experiment.

Of the five structures in Figure 3, three can be dismissed as qualitatively in disagreement with the ENDOR results: P-7, $E_4(3H;CH)$, and $E_4(4H)^{(b)}$. Indeed, P-7 has the wrong electron count (7 not $4[e^-/H^+]$) and is not even an odd-electron, EPR-active state. Neither of the other two contains two bridging hydrides, much less two that can exhibit the signature rhombic, coaxial, and permuted anisotropic hyperfine coupling tensors, while the ^1H of the protonated carbide of $E_4(3H;CH)$ and other such models would fail to show the large measured isotropic coupling. A third structure, $E_4(4H)^{(c)}$, does exhibit two hydrides, both of which bridge the same pair of Fe ions (Fe2 and Fe6), but the resulting relative orientations of the two hydride dipolar tensors are in strong quantitative disagreement with those found experimentally.

Only the $E_4(4H)^{(a)}$ structure can accurately account for the observed presence of two bridging hydrides with rhombic anisotropic tensors that are coaxial but with permuted tensor components (Table 2). Taken together, these results allow us to assign $E_4(4H)^{(a)}$, with $[Fe2-H-Fe6]$ and $[Fe3-H-Fe7]$ hydride bridges whose planes are essentially perpendicular to the Fe2,3,6,7 FeMo-co face and parallel to each other (Figure 3), as the lowest-energy FeMo-co state of the Janus intermediate, trapped during the relatively slow hand-freezing process used to generate the samples for ENDOR measurements. Although these measurements were performed at 2 K, EPR spectra indicate that no other isomer of Janus becomes populated by ~25 K[12,14] (above which the signal becomes relaxation-broadened). However, because calculations have indicated the presence of isomers, such as $E_4(4H)^{(b/c)}$ (Figure 3), very close in energy, we can envision that at ambient temperature the $E_4(4H)$ hydrides may become fluxional, with a dynamic population of multiple isomers.

■ ASSOCIATED CONTENT

Ⓢ Supporting Information

The Supporting Information is available free of charge on the ACS Publications website at DOI: 10.1021/jacs.9b04474.

> ENDOR spectra, simulations, and related parameters (PDF)

■ AUTHOR INFORMATION

Corresponding Authors
*lance.seefeldt@usu.edu

*simone.raugei@pnnl.gov
*bmh@northwestern.edu

ORCID

David A. Case: 0000-0003-2314-2346
Lance C. Seefeldt: 0000-0002-6457-9504
Simone Raugei: 0000-0001-9118-8480
Brian M. Hoffman: 0000-0002-3100-0746

Notes

The authors declare no competing financial interest.

REFERENCES

(1) Doan, P. E.; Gurbiel, R. J.; Hoffman, B. M. The Ups and Downs of Feher-Style ENDOR. *Appl. Magn. Reson.* **2007**, *31*, 649−663.

(2) Burgess, B. K.; Lowe, D. J. Mechanism of Molybdenum Nitrogenase. *Chem. Rev.* **1996**, *96*, 2983−3012.

(3) Seefeldt, L. C.; Hoffman, B. M.; Dean, D. R. Mechanism of Mo-Dependent Nitrogenase. *Annu. Rev. Biochem.* **2009**, *78*, 701−722.

(4) Thorneley, R. N. F.; Lowe, D. J. Kinetics and Mechanism of the Nitrogenase Enzyme System. *Metal Ions Biol.* **1985**, *7*, 221−284.

(5) Wilson, P. E.; Nyborg, A. C.; Watt, G. D. Duplication and Extension of the Thorneley and Lowe Kinetic Model for *Klebsiella Pneumoniae* Nitrogenase Catalysis Using a Mathematica Software Platform. *Biophys. Chem.* **2001**, *91*, 281−304.

(6) Lukoyanov, D.; Barney, B. M.; Dean, D. R.; Seefeldt, L. C.; Hoffman, B. M. Connecting Nitrogenase Intermediates with the Kinetic Scheme for N₂ Reduction by a Relaxation Protocol and Identification of the N₂ Binding State. *Proc. Natl. Acad. Sci. U. S. A.* **2007**, *104*, 1451−1455.

(7) Hoffman, B. M.; Lukoyanov, D.; Dean, D. R.; Seefeldt, L. C. Nitrogenase: A Draft Mechanism. *Acc. Chem. Res.* **2013**, *46*, 587−595.

(8) Lukoyanov, D.; Yang, Z. Y.; Duval, S.; Danyal, K.; Dean, D. R.; Seefeldt, L. C.; Hoffman, B. M. A Confirmation of the Quench-Cryoannealing Relaxation Protocol for Identifying Reduction States of Freeze-Trapped Nitrogenase Intermediates. *Inorg. Chem.* **2014**, *53*, 3688−3693.

(9) Igarashi, R. Y.; Laryukhin, M.; Dos Santos, P. C.; Lee, H. I.; Dean, D. R.; Seefeldt, L. C.; Hoffman, B. M. Trapping H⁻ Bound to the Nitrogenase FeMo-Cofactor Active Site During H2 Evolution: Characterization by ENDOR Spectroscopy. *J. Am. Chem. Soc.* **2005**, *127*, 6231−6241.

(10) Crabtree, R. H. *The Organometallic Chemistry of the Transition Metals*, 5th ed.; Wiley: Hoboken, NJ, 2009.

(11) Peruzzini, M.; Poli, R.; Eds. *Recent Advances in Hydride Chemistry*; Elsevier Science B.V.: Amsterdam, The Netherlands, 2001.

(12) Hoffman, B. M.; Lukoyanov, D.; Yang, Z. Y.; Dean, D. R.; Seefeldt, L. C. Mechanism of Nitrogen Fixation by Nitrogenase: The Next Stage. *Chem. Rev.* **2014**, *114*, 4041−4062.

(13) Lukoyanov, D.; Khadka, N.; Yang, Z. Y.; Dean, D. R.; Seefeldt, L. C.; Hoffman, B. M. Reductive Elimination of H₂ Activates Nitrogenase to Reduce the N≡N Triple Bond: Characterization of the E4(4H) Janus Intermediate in Wild-Type Enzyme. *J. Am. Chem. Soc.* **2016**, *138*, 10674−10683.

(14) Raugei, S.; Seefeldt, L. C.; Hoffman, B. M. Critical Computational Analysis Illuminates the Reductive-Elimination Mechanism That Activates Nitrogenase for N₂ Reduction. *Proc. Natl. Acad. Sci. U. S. A.* **2018**, *115*, No. E10521.

(15) Lukoyanov, D.; Khadka, N.; Dean, D. R.; Raugei, S.; Seefeldt, L. C.; Hoffman, B. M. Photoinduced Reductive Elimination of H₂ from the Nitrogenase Dihydride (Janus) State Involves a FeMo-Cofactor-H₂ Intermediate. *Inorg. Chem.* **2017**, *56*, 2233−2240.

(16) Cao, L.; Caldararu, O.; Ryde, U. Protonation and Reduction of the FeMo Cluster in Nitrogenase Studied by Qm/Mm Calculations. *J. Chem. Theory Comput.* **2018**, *14*, 6653.

(17) Cao, L.; Ryde, U. Extremely Large Differences in Dft Energies for Nitrogenase Models. *Phys. Chem. Chem. Phys.* **2019**, *21*, 2480−2488.

(18) Bjornsson, R.; Lima, F. A.; Spatzal, T.; Weyhermüller, T.; Glatzel, P.; Bill, E.; Einsle, O.; Neese, F.; DeBeer, S. Identification of a Spin-Coupled Mo(Iii) in the Nitrogenase Iron−Molybdenum Cofactor. *Chemical Science* **2014**, *5*, 3096−3103.

(19) Bjornsson, R.; Neese, F.; DeBeer, S. Revisiting the Mössbauer Isomer Shifts of the FeMoco Cluster of Nitrogenase and the Cofactor Charge. *Inorg. Chem.* **2017**, *56*, 1470−1477.

(20) Willems, J.-P.; Lee, H.-I.; Burdi, D.; Doan, P. E.; Stubbe, J.; Hoffman, B. M. Identification of the Protonated Oxygenic Ligands of Ribonucleotide Reductase Intermediate X by Q-Band ¹,²h Cw and Pulsed ENDOR. *J. Am. Chem. Soc.* **1997**, *119*, 9816−9824.

(21) Randall, D. W.; Gelasco, A.; Caudle, M. T.; Pecoraro, V. L.; Britt, R. D. Ese-ENDOR and Eseem Characterization of Water and Methanol Ligation to a Dinuclear Mn(III)Mn(IV) Complex. *J. Am. Chem. Soc.* **1997**, *119*, 4481−4491.

(22) Lukoyanov, D.; Yang, Z.-Y.; Dean, D. R.; Seefeldt, L. C.; Hoffman, B. M. Is Mo Involved in Hydride Binding by the Four-Electron Reduced (E₄) Intermediate of the Nitrogenase MoFe Protein? *J. Am. Chem. Soc.* **2010**, *132*, 2526−2527.

(23) Kinney, R. A.; Saouma, C. T.; Peters, J. C.; Hoffman, B. M. Modeling the Signatures of Hydrides in Metalloenzymes: ENDOR Analysis of a Di-Iron Fe(Mu-Nh)(Mu-H)Fe Core. *J. Am. Chem. Soc.* **2012**, *134*, 12637−12647.

(24) Kinney, R. A.; Hetterscheid, D. G. H.; Hanna, B. S.; Schrock, R. R.; Hoffman, B. M. Formation of {[HIPTN₃N]Mo(III)H}⁻ by Heterolytic Cleavage of H₂ as Established by EPR and ENDOR Spectroscopy. *Inorg. Chem.* **2010**, *49*, 704−713.

(25) Yang, H.; Rittle, J.; Marts, A. R.; Peters, J. C.; Hoffman, B. M. ENDOR Characterization of (N₂)Feᴵᴵ(µ-H)₂Feᴵ(N₂)-: A Spectroscopic Model for N₂ Binding by the Di-µ-Hydrido Nitrogenase Janus Intermediate. *Inorg. Chem.* **2018**, *57*, 12323−12330.

(26) Sippel, D.; Einsle, O. The Structure of Vanadium Nitrogenase Reveals an Unusual Bridging Ligand. *Nat. Chem. Biol.* **2017**, *13*, 956−960.

(27) Rohde, M.; Sippel, D.; Trncik, C.; Andrade, S. L. A.; Einsle, O. The Critical E4 State of Nitrogenase Catalysis. *Biochemistry* **2018**, *57*, 5497−5504.

(28) Siegbahn, P. E. M. Is There Computational Support for an Unprotonated Carbon in the E₄ State of Nitrogenase? *J. Comput. Chem.* **2018**, *39*, 743−747.

(29) Siegbahn, P. E. M. Model Calculations Suggest That the Central Carbon in the FeMo-Cofactor of Nitrogenase Becomes Protonated in the Process of Nitrogen Fixation. *J. Am. Chem. Soc.* **2016**, *138*, 10485−10495.

(30) McKee, M. L. A New Nitrogenase Mechanism Using a CFe₈F₉ Model: Does H₂ Elimination Activate the Complex to N₂ Addition to the Central Carbon Atom? *J. Phys. Chem. A* **2016**, *120*, 754−764.

(31) Rao, L.; Xu, X.; Adamo, C. Theoretical Investigation on the Role of the Central Carbon Atom and Close Protein Environment on the Nitrogen Reduction in Mo Nitrogenase. *ACS Catal.* **2016**, *6*, 1567−1577.

(32) Bruggemann, W.; Niklas, J. R. Stochastic ENDOR. *J. Magn. Reson., Ser. A* **1994**, *108*, 25−29.

(33) Doan, P. E. Combining Steady-State and Dynamic Methods for Determining Absolute Signs of Hyperfine Interactions: Pulsed ENDOR Saturation and Recovery (Pestre). *J. Magn. Reson.* **2011**, *208*, 76−86.

(34) Lukoyanov, D. A.; Khadka, N.; Yang, Z.-Y.; Dean, D. R.; Seefeldt, L. C.; Hoffman, B. M. Hydride Conformers of the Nitrogenase FeMo-Cofactor Two-Electron Reduced State E_2(2H), Assigned Using Cryogenic Intra Electron Paramagnetic Resonance Cavity Photolysis. *Inorg. Chem.* **2018**, *57*, 6847−6852.

(35) Christiansen, J.; Goodwin, P. J.; Lanzilotta, W. N.; Seefeldt, L. C.; Dean, D. R. Catalytic and Biophysical Properties of a Nitrogenase Apo-MoFe Protein Produced by a *Nifb*-Deletion Mutant of *Azotobacter Vinelandii*. *Biochemistry* **1998**, *37*, 12611−12623.

(36) Werst, M. M.; Davoust, C. E.; Hoffman, B. M. Ligand Spin Densities in Blue Copper Proteins by Q-Band ^{1}H and ^{14}N ENDOR Spectroscopy. *J. Am. Chem. Soc.* **1991**, *113*, 1533−1538.

(37) Feher, G. Electron Spin Resonance Experiments on Donors in Silicon. I. Electronic Structure of Donors by the Electron Nuclear Double Resonance Technique. *Phys. Rev.* **1959**, *114*, 1219−1244.

(38) Feher, G. Observation of Nuclear Magnetic Resonances Via the Electron Spin Resonance Line. *Phys. Rev.* **1956**, *103*, 834−835.

(39) Brueggemann, W.; Niklas, J. R. Stochastic ENDOR. *J. Magn. Reson., Ser. A* **1994**, *108*, 25−29.

(40) Hoffman, B. M.; DeRose, V. J.; Ong, J. L.; Davoust, C. E. Sensitivity Enhancement in Field-Modulated Cw ENDOR Via RF Bandwidth Broadening. *J. Magn. Reson., Ser. A* **1994**, *110*, 52−57.

(41) Schweiger, A.; Jeschke, G. *Principles of Pulse Electron Paramagnetic Resonance*; Oxford University Press: Oxford, U.K., 2001.

(42) Davoust, C. E.; Doan, P. E.; Hoffman, B. M. Q-Band Pulsed Electron Spin-Echo Spectrometer and Its Application to ENDOR and Eseem. *J. Magn. Reson., Ser. A* **1996**, *119*, 38−44.

(43) Hoffman, B. M.; Martinsen, J.; Venters, R. A. General-Theory of Polycrystalline ENDOR Patterns - g and Hyperfine Tensors of Arbitrary Symmetry and Relative Orientation. *J. Magn. Reson.* **1984**, *59*, 110−123.

(44) Hoffman, B. M. Electron Nuclear Double Resonance (ENDOR) of Metalloenzymes. *Acc. Chem. Res.* **1991**, *24*, 164−170.

(45) Doan, P. E.: The Past, Present, and Future of Orientation-Selected ENDOR Analysis: Solving the Challenges of Dipolar-Coupled Nuclei. In *Paramagnetic Resonance of Metallobiomolecules*; Telser, J., Ed.; American Chemical Society: Washington, D.C., 2003; pp 55−81.

(46) Stoll, S.; Schweiger, A. Easyspin, a Comprehensive Software Package for Spectral Simulation and Analysis in EPR. *J. Magn. Reson.* **2006**, *178*, 42−55.

(47) Sippel, D.; Rohde, M.; Netzer, J.; Trncik, C.; Gies, J.; Grunau, K.; Djurdjevic, I.; Decamps, L.; Andrade, S. L. A.; Einsle, O. A Bound Reaction Intermediate Sheds Light on the Mechanism of Nitrogenase. *Science* **2018**, *359*, 1484−1489.

(48) Equation 4a was suggested for clarity by a knowledgeable reviewer. Equations 4b−4d are from ref 20, with β_2 here being the complement of β_2 defined there, noting, however, that for a given geometry one can express tensor components in terms of any two geometric parameters and the law of cosines, as expressly noted in ref 21.

(49) For completeness, we note that no state in which the two hydrides share a common vertex (cv), such as one bridging Fe2 and Fe6 and the second bridging Fe2 and Fe3, has been found in BS-DFT computations even at extremely high energies, so such structures are not considered.

(50) Spatzal, T.; Aksoyoglu, M.; Zhang, L. M.; Andrade, S. L. A.; Schleicher, E.; Weber, S.; Rees, D. C.; Einsle, O. Evidence for Interstitial Carbon in Nitrogenase FeMo Cofactor. *Science* **2011**, *334*, 940−940.